COMMUN. MATH. SCI.
Vol. 15, No. 7, pp. 2027–2054

OPTIMIZED QUASICONFORMAL PARAMETERIZATION WITH USER-DEFINED AREA DISTORTIONS*

KA CHUN LAM† AND LOK MING LUI‡

Abstract. Parameterization, a process of mapping a complicated domain onto a simple canonical domain, is crucial in different areas such as computer graphics, medical imaging and scientific computing. Conformal parameterization has been widely used since it preserves the local geometry well. However, a major drawback is the area distortion introduced by the conformal parameterization, causing inconvenience in many applications such as texture mapping in computer graphics or visualization in medical imaging. This work proposes a remedy to construct a parameterization that balances between conformality and area distortions. We present a variational algorithm to compute the optimized quasiconformal parameterization with controllable area distortions. The distribution of the area distortion can be prescribed by users according to the application. The main strategy is to minimize a combined energy functional consisting of an area mismatching term and a regularization term involving the Beltrami coefficient of the map. The Beltrami coefficient controls the conformality of the parameterization. Landmark constraints can be incorporated into the model to obtain landmark-aligned parameterization. Experiments have been carried out on both synthetic and real data. Results demonstrate the efficacy of the proposed algorithm to compute the optimized parameterization with controllable area distortion while preserving the local geometry as well as possible.

Keywords. Area-preserving mapping; Beltrami coefficient, conformality distortion; parameterization, texture mapping.

AMS subject classifications. 65D18; 65K10; 92C55.

1. Introduction

Surface parameterization of 3D geometric objects has central importance in various fields, such as computer graphics, medical imaging and scientific computing. It refers to the process of mapping a surface one-to-one and onto a simple parameter domain. It has been widely used in different applications, including texture mapping, shape analysis, geometry processing, surface classification and recognition. Recently, various surface parameterization techniques have been developed.

In general, surface parameterization introduces different kinds of distortions. Depending on applications, different parameterization algorithms aim to minimize different types of distortions. For example, isometric parameterization aims to preserve the metric tensor. Authalic projection minimizes the area distortion under the parameterization. Amongst the various parameterization techniques, conformal parameterization has been extensively used, since it preserves angles and hence the local geometry well. However, a major drawback is the area distortion introduced by the parameterization. Although angles are preserved, some regions on the surface can be seriously squeezed on the parameter domain. This leads to problems in some practical applications in scientific computing and computer graphics. For instance, in computer graphics, surface conformal parameterizations can be used for texture mapping. The goal is to project a 2D image onto the surface to increase the realism of the 3D model. When there is a huge area distortion under the texture map, the projected texture on the surface

*Received: August 18, 2016; accepted (in revised form): June 27, 2017. Communicated by Wotao Yin.

†Department of Mathematics, The Chinese University of Hong Kong, Shatin, Hong Kong (kclam@math.cuhk.edu.hk).

‡Department of Mathematics, The Chinese University of Hong Kong, Shatin, Hong Kong (lmlui@math.cuhk.edu.hk).

may look unnatural (see Figure 6.7(b)). In practice, it is more desirable to obtain a parameterization whose distortions are controllable by users.

In this paper, we propose a new approach to construct an optimized quasiconformal parameterization with controllable area distortions. Depending on the specific application, the distribution of the area distortion under the parameterization can be prescribed by users. Our goal is to find an optimized parameterization from the surface onto a simple domain, such that the area distortion follows the prescribed distribution as much as possible while minimizing the local geometric distortion. The main strategy is by minimizing a combined energy functional involving an area distortion term and the Beltrami coefficient of the mapping. The Beltrami coefficient term aims to control the conformality distortion and hence the local geometric distortion under the parameterization. The area term involving the logarithm of Jacobian aims to control the area distortion under the mapping. Parameters in the energy model can be adjusted by users to balance between the conformality and area distortions. Sometimes, landmark features of the surface are required to be projected to desired locations. For this purpose, landmark constraints can also be incorporated in our proposed model. In this work, we propose to apply a splitting method to minimize the proposed energy functional, which alternatively optimizes the energy terms involving the Beltrami coefficient and the mapping respectively. Experiments have been carried out to parameterize different surface models. Results demonstrate the efficacy of our proposed method to compute an optimized parameterization that preserves both local geometry and area distortion as well as possible. Applications of the proposed parameterization method in computer graphics and medical imaging are also shown.

In short, the contributions of this paper are threefold. Firstly, we propose a variational approach to construct the optimized quasiconformal parameterization with controllable area distortion while minimizing the conformality (local geometric) distortion. Our formulation is general and flexible, which allows users to define a desired distribution of area distortion according to their specific applications. The method can also be applied to high-genus surfaces. Secondly, we propose to incorporate the Beltrami coefficients into the model, by which both smoothness and bijectivity of the parameterization can be effectively achieved. Thirdly, we propose to incorporate feature landmarks into the model to compute a meaningful parameterization with consistent feature alignment.

The rest of the paper is organized as follows. In Section 2, we describe some previous works closely related to our paper. In Section 3, we introduce the basic mathematical concepts about the conformal and quasi-conformal geometry. In Section 4, our proposed parameterization model is described in details. The numerical implementation of the proposed model is explained in Section 5. Experimental results are shown in Section 6. Conclusion and future works are discussed in Section 7.

2. Previous work

In this section, we give an overview of some previous works closely related to the paper.

2.1. Conformal parameterization. Surface conformal parameterization has been widely used. It minimizes angular distortions and hence preserves the local geometry well. Different algorithms for computing conformal parameterizations have been developed in recent years [7–10, 12, 16, 32, 34]. For example, Hurdal et al. [10] proposed to compute brain conformal parameterizations using circle packing and applied them to registration of human brains. Gu et al. [7, 8, 12, 32] proposed to compute surface conformal parameterizations using harmonic energy minimization, holomorphic 1-forms and curvature flow. Haker et al. [9] applied the conformal surface parameterization to

obtain angle preserving texture mapping. Although conformal parameterizations preserve the local geometry well, they generally cannot cope with feature correspondence and may cause severe area distortions.

2.2. Area preserving parameterization. Several works have been done on flattening surfaces with the area preserving constraint. Dominitz et al. [3] applied the optimal mass transport technique to find the area preserving parameterization, which was used for texture mapping. Zhao et al. [35] improved the efficiency of the optimal mass transport technique to find the area-preserving flattening, which is based on the Monge–Brenier theory. Zou et al. [36] proposed to use Lie advection to compute the area preserving surface mapping. However, all the above methods do not handle prescribed landmark constraints. Moreover, conformality distortions are often introduced, and hence the local geometry is usually not preserved under the parameterization.

2.3. Feature point mapping. Landmark-based registration has also been widely studied and different algorithms have been proposed. Bookstein et al. [1] proposed to use the thin-plate spline regularization (or biharmonic regularization) to obtain a registration that matches landmarks as much as possible. Tosun et al. [30] proposed to combine the iterative closest point registration, the parametric relaxation and the inverse stereographic projection to align cortical sulci across brain surfaces. These diffeomorphisms obtained can better match landmark features, although not perfectly. Wang et al. [21, 22, 24] proposed to compute the optimized harmonic registrations of brain cortical surfaces. The main idea is to minimize a compounded energy involving a landmark-mismatching term [23]. The obtained registration is an optimized harmonic map that better aligns landmarks. However, landmarks are not exactly matched and bijectivity cannot be guaranteed under large number of landmark constraints. To secure the bijectivity of the mapping, Joshi et al. [6] proposed the large deformation diffeomorphic metric mapping (LDDMM) to register images with a large deformation. The registration mapping can be shown to lie in the space of diffeomorphisms. Following this work, Glaunés et al. [5, 6, 31] proposed to generate large deformation diffeomorphisms with given displacements of a finite set of template landmarks. The time dependent vector fields are useful for the computation of registration with large deformations, although the computational cost of the algorithm is more expensive. For the above methods, although landmarks can be aligned, they generally cannot control conformality and area distortions.

Quasi-conformal mapping that matches landmarks consistently has also been proposed [13, 18, 20, 25]. Wei et al. [33] proposed to compute landmark-matching quasiconformal mappings for human face registration. The Beltrami coefficient associated to a landmark-matching parameterization is approximated. However, neither exact landmark matching nor the bijectivity of the mapping can be ensured when large deformations occur. Later, Lam et al. [14] proposed an iterative scheme, which provides an efficient way to obtain an exact landmark matching bijective registration even with large deformations. The above algorithms can obtain parameterizations, which align landmarks while minimizing the conformality distortions. However, area distortions cannot be controlled. To deal with different situations, Schüller et al. [27] proposed an effective algorithm, which modifies different deformation energies, like the as-rigid-as-possible (ARAP), Green's strain or conformal energy, to guarantee local injectivity of the mapping. Locally injective planar or volumetric piecewise-linear maps can be obtained using a barrier term to prevent elements from flipping. Since flipping is prohibited by the barrier function, the obtained registration map lies inside the class of quasiconformal mappings. Lipman et al. [17] also introduced an algorithm to compute

bounded distortion mappings, which prevents flipping by controlling the singular values of the transformation on each element. With the freedom of choosing different deformation energies, these methods can be combined with a suitable area distortion term to obtain a parameterization with less area distortion. Nevertheless, it is observed that the approach by solving Beltrami's equation is easier to control the bijectivity and smoothness via adjusting the Beltrami coefficients directly. In addition, there is an one-one correspondence between the set of all Beltrami coefficients (with sup-norm less than 1) and the set of all quasi-conformal homeomorphisms. Thus, the approach by adjusting the Beltrami coefficients indeed considers the whole class of quasiconformal homeomorphisms. As a result, unlike other approaches, the reduction of the mapping class is not required. Motivated by the above, we adopt the approach by solving Beltrami's equation in this work.

3. Mathematical background

In this section, we describe some basic mathematical concepts related to our algorithms. For details, we refer the readers to [4, 15, 26].

A surface S with a conformal structure is called a *Riemann surface*. Given two Riemann surfaces M and N, a map $f: M \to N$ is *conformal* if it preserves the surface metric up to a multiplicative factor called the *conformal factor*. An immediate consequence is that every conformal map preserves angles. With the angle-preserving property, a conformal map effectively preserves the local geometry of the surface structure.

A generalization of conformal maps is the *quasi-conformal* maps, which are orientation preserving homeomorphisms between Riemann surfaces with bounded conformality distortion, in the sense that their first order approximations takes infinitestimal circles to infinitestimal ellipses of bounded eccentricity [4]. Mathematically, $f: \mathbb{C} \to \mathbb{C}$ is quasi-conformal provided that it satisfies the Beltrami equation

$$\frac{\partial f}{\partial \overline{z}} = \mu(z) \frac{\partial f}{\partial z} \tag{3.1}$$

for some complex-valued function μ satisfying $||\mu||_\infty < 1$. μ is called the *Beltrami coefficient*, which is a measure of non-conformality. It measures how far the map at each point is deviated from a conformal map. In particular, the map f is conformal at p when $\mu(p) = 0$. In other words, f is angle-preserving at p when $\mu(p) = 0$. Infinitesimally, around a point p, f may be expressed with respect to its local parameter as follows:

$$\begin{aligned} f(z+p) &\approx f(p) + f_z(p) z + f_{\overline{z}}(p) \overline{z} \\ &= f(p) + f_z(p)(z + \mu(p)\overline{z}). \end{aligned} \tag{3.2}$$

Obviously, f is not conformal if and only if $\mu(p) \neq 0$. Inside the local parameter domain, f may be considered as a map composed of a translation to $f(p)$ together with a stretch map $S(z) = z + \mu(p)\overline{z}$, which is post-composed by a multiplication of $f_z(p)$, which is conformal. All the conformal distortion of $S(z)$ is caused by $\mu(p)$. $S(z)$ is the map that causes f to map a small circle to a small ellipse. From $\mu(p)$, we can determine the angles of the directions of maximal magnification and shrinking and the amount of them as well. Specifically, the angle of maximal magnification under the stretch map is $\arg(\mu(p))/2$ with magnifying factor $1 + |\mu(p)|$. The angle of maximal shrinking under the stretch map is the orthogonal angle $(\arg(\mu(p)) - \pi)/2$ with shrinking factor $1 - |\mu(p)|$. Thus, the Beltrami coefficient μ gives us important information about the properties of the map (See Figure 3.1).

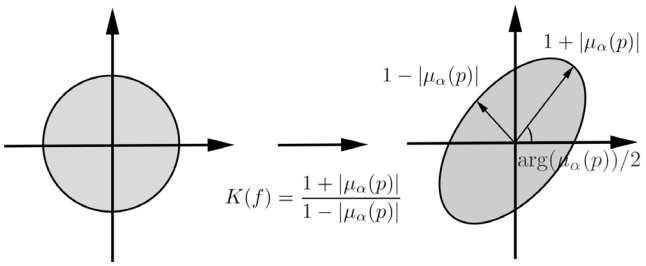

Fig. 3.1: *Illustration of the relationship between a quasi-conformal map and its Beltrami coefficient.*

The maximal dilation of f is given by:

$$K(f)=\frac{1+||\mu||_\infty}{1-||\mu||_\infty}. \tag{3.3}$$

4. Proposed model

In this section, we describe our proposed variational model for the optimized quasiconformal parameterization with controllable area distortion in details.

4.1. Problem setting. Let S be a simply-connected open surface. Suppose $D\subset\mathbb{R}^2$ is our target parameter domain, which can either be a 2D rectangle or a unit disk $\mathbb{D}$. Our goal is to look for an optimized parameterization $\varphi: S\to D$, which satisfies the prescribed area distribution and minimizes the conformality distortion as well as possible.

Mathematically, our problem can be formulated as follows:

$$\begin{aligned} &\underset{\varphi:S\to D}{\text{minimize}} && E(\varphi) \\ &\text{subject to} && J(\varphi)\big|_{\Omega_i}=\lambda_i,\, i=1,\dots,m, \end{aligned} \tag{4.1}$$

where $E(\varphi)$ is an energy functional that controls the local geometric distortion under φ. $J(\varphi)$ is the Jacobian determinant of $\varphi: S\to D$, which can be defined using the coordinate chart of S. Let $\phi_p: U_p\to\mathbb{R}^2$ be a conformal coordinate chart of a neighbourhood U_p of $p\in S$. Then, $J(\varphi)(p)$ can be obtained by

$$J(\varphi)(p)=c_{\phi_p}(p)J(\varphi\circ\phi_p^{-1})(p), \tag{4.2}$$

where c_{ϕ_p} is the conformal factor of ϕ_p and $J(\varphi\circ\phi_p^{-1})$ is the usual Jacobian determinant of the mapping $\varphi\circ\phi_p^{-1}$. Ω_i's are the subdomains of S and λ_i is the prescribed area distribution on Ω_i.

Note that both λ_i and Ω_i are user-defined. We assume the area distribution λ_i is prescribed according to the following condition:

$$\mathcal{A}(D)-\sum_{i=1}^{m}\int_{\Omega_i}\lambda_i dA\begin{cases}=0 & \text{if } \bigcup_{i=1}^m\Omega_i=S\\ >0 & \text{if } \bigcup_{i=1}^m\Omega_i\subset S\end{cases}, \tag{4.3}$$

where $\mathcal{A}(D)$ is the total area of the parameter domain D.

The above condition ensures the area distribution is correctly prescribed. More specifically, the prescribed total area of the sub-domains Ω_i's must be smaller than the

total area of D. In practice, we normalize the area of D such that it has the same area as the surface area of S. When $\lambda_i = 1$, the area of Ω_i is supposed to be preserved under the parameterization. On the other hand, Ω_i is expected to be expanded or squeezed on the parameter domain D under the parameterization if $\lambda_i > 1$ or $\lambda_i < 1$ respectively. Therefore, users can prescribe their desired area distortions under the parameterization according to their applications.

In some situations, one might want to parameterize S in such a way that feature landmarks on S are aligned to prescribed locations in D. This type of parameterization is called the *landmark-aligned* parameterization. For example, in computer graphics, a landmark aligned parameterization is required for an accurate texture mapping. For this purpose, the aforementioned model can be extended to compute a landmark-aligned optimized quasiconformal parameterization with controllable area distortion. Denote the corresponding landmark constraints by $\{p_i \in S\}_{i=1}^n \leftrightarrow \{q_i \in D\}_{i=1}^n$. We require that $\varphi(p_i) = q_i$ for $1 \le i \le n$. The extended model can be formulated as follows:

$$\begin{aligned} \underset{\varphi: S \to D}{\text{minimize}} \quad & E(\varphi) \\ \text{subject to} \quad & \varphi(p_i) = q_i,\ i = 1, \ldots, n \\ & J(\varphi)\big|_{\Omega_i} = \lambda_i,\ i = 1, \ldots, m. \end{aligned} \tag{4.4}$$

4.2. Energy model. In this subsection, we describe how we can set the energy functional E to control the local geometric distortion of the parameterization.

The local geometric distortion can be described by its conformality distortion. The conformality distortion of a parameterization $\varphi: S \to D$ can be measured by its Beltrami differential, which is a collection of Beltrami coefficients with respect to different coordinate charts of S. For any $p \in S$, the Beltrami coefficient $\mu(\varphi)(p)$ at p with respect to a conformal coordinate chart $\phi_p: U_p \to \mathbb{R}^2$ is given by

$$\mu(\varphi)(p) = \frac{\partial \tilde{\varphi}}{\partial \bar{z}}(z_p) \Big/ \frac{\partial \tilde{\varphi}}{\partial z}(z_p), \tag{4.5}$$

where $\tilde{\varphi} := \varphi \circ \phi_p^{-1}$ is a mapping in $\mathbb{R}^2$ and $z_p = \phi_p(p)$. In other words, $\mu(\varphi)(p)$ is a complex number. In particular, a local conformal parameterization ϕ_p on the chart U_p is introduced. Note that the argument of $\mu(\varphi)$ depends on the conformal coordinate chart ϕ_p. However, its magnitude $|\mu(\varphi)(p)|$ is invariant under different choices of conformal coordinate chart. In fact, let $\tilde{\varphi}_1 = \varphi \circ \phi_1^{-1}$ and $\tilde{\varphi}_2 = \varphi \circ \phi_2^{-1}$, where ϕ_1 and ϕ_2 are two different coordinate charts of S. Denote $\phi_2 \circ \phi_1^{-1}$ (on a well-defined region) by Φ, which is conformal. Also, we denote $\mu_1(\varphi)$ and $\mu_1(\varphi)$ to be the Beltrami coefficients of φ with respect to the coordinate charts ϕ_1 and ϕ_2 respectively. Then, by simple calculation, we obtain

$$\mu_1(\varphi) = \frac{\partial \tilde{\varphi}_1}{\partial \bar{z}} \Big/ \frac{\partial \tilde{\varphi}_1}{\partial z} = \frac{\partial \tilde{\varphi}_2 \circ \Phi}{\partial \bar{z}} \Big/ \frac{\partial \tilde{\varphi}_2 \circ \Phi}{\partial z} = \frac{\overline{\Phi_z}}{\Phi_z} \mu_2(\varphi) \circ \Phi. \tag{4.6}$$

Hence, $|\mu_1(\varphi)| = |\mu_2(\varphi) \circ \Phi| = |\mu_2(\varphi)|$ and their arguments differ by $\frac{\overline{\Phi_z}}{\Phi_z}$. In practice, we compute $\mu(\varphi)$ with a global conformal parameterization of S. In the following, since we are mainly concerned about the magnitude (rather than the arguments) of the Beltrami coefficient, we assume that $\mu(\varphi)$ of a parameterization is measured with respect to a given global conformal parameterization ϕ.

A parameterization φ is conformal at p if and only if $\mu(\varphi)(p) = 0$. This motivates us to look for φ that minimizes $|\mu(\varphi)|$. Hence, we define the energy functional E as

follows:

$$E(\varphi)=\int_S|\mu(\varphi)|^2+\int_S|\nabla\mu(\varphi)|^2. \tag{4.7}$$

The first energy term aims to minimize the conformality distortion. The second energy term is a regularization term that enhances the smoothness of φ.

To simplify the problem, we eliminate the hard constraint $J(\varphi)\big|_{\Omega_i}=\lambda_i$ by incorporating it into the energy functional

$$\widetilde{E}(\varphi)=\int_S|\mu(\varphi)|^2+\int_S|\nabla\mu(\varphi)|^2+\alpha\left(\sum_{i=1}^m\int_{\Omega_i}|\log J(\varphi)-\log\lambda_i|^2\right). \tag{4.8}$$

Here, α is called the penalty parameter. It controls how well the parameterization φ follows the prescribed area distribution. If α is set to be large, φ follows the prescribed area distortion more in the cost of losing the conformality. When α is small, the first two energy terms are more dominant. Thus, more conformality and smoothness can be achieved, however, φ follows the prescribed area distribution less.

Furthermore, φ is required to be bijective. The bijectivity of φ can be controlled by $|\mu(\varphi)|$. In fact, $||\mu(\varphi)||_\infty<1$ if and only if φ is bijective. This fact can be observed from the following theorem.

THEOREM 4.1. *Suppose $\mu:\Omega\to\mathbb{C}$ be a complex-valued function defined on a simply-connected open set $\Omega\subset\mathbb{C}$ satisfying $||\mu||_\infty<1$. Then, its associated quasiconformal map $f^\mu:\Omega\to D$ is bijective, where $D:=f^\mu(\Omega)$. Conversely, if $f^\mu:\Omega\to D$ is an orientation-preserving homeomorphism, then $||\mu||_\infty<1$.*

Proof. Please refer to [4] and [14]. ∎

Suppose S is a simply-connected open surface. S can be globally and conformally parameterized by $\phi:S\to D\subset\mathbb{C}$. Then, $||\mu(\varphi)||_\infty<1$ if and only if $||\mu(\varphi\circ\phi^{-1})||_\infty<1$. This implies $\varphi\circ\phi^{-1}$ is a bijection by Theorem 4.1 and hence φ is a bijection.

Our optimization problem can now be formulated as follows:

$$\begin{aligned}&\underset{\varphi:S\to D}{\text{minimize}} \quad \widetilde{E}(\varphi):=\int_S|\mu(\varphi)|^2+\int_S|\nabla\mu(\varphi)|^2+\alpha\left(\sum_{i=1}^m\int_{\Omega_i}|\log J(\varphi)-\log\lambda_i|^2\right)\\ &\text{subject to} \quad (1)\ \varphi(p_i)=q_i,\ i=1,\dots,n\\ &\qquad\qquad\ (2)\ \|\mu(\varphi)\|_\infty<1.\end{aligned} \tag{4.9}$$

The above variational model (4.9) enforces hard landmark constraints. Sometimes, it may be more suitable to enforce soft landmark constraints, which allows certain degree of landmark mismatching. This situation occurs when landmarks cannot be precisely located. In the situation when exact landmark matching is not necessary, enforcing soft landmark constraints allows more conformality to be achieved. Model (4.9) can be easily modified to a variational model with soft landmark constraints by minimizing

$$\widetilde{E}_{soft}(\varphi)=\int_S|\mu(\varphi)|^2+\int_S|\nabla\mu(\varphi)|^2+\alpha\left(\sum_{i=1}^m\int_{\Omega_i}|\log J(\varphi)-\log\lambda_i|^2\right)+\beta\sum_{i=1}^n|\varphi(p_i)-q_i|^2 \tag{4.10}$$

subject to the constraint that $\|\mu(\varphi)\|_\infty<1$.

Note that minimizing the above variational models (4.9) or (4.10) over φ is challenging. In particular, $\mu(\varphi)$ is defined as the quotient of first derivatives of φ, whereas $\nabla\mu(\varphi)$ involves the second derivatives of φ. The Euler–Lagrange equations of the energy functionals are complicated. To alleviate this issue, we simplify our optimization process using the splitting method. Note that the original model (4.9) is equivalent to minimizing

$$\widetilde{E}'(\nu,\varphi)=\int_S|\nu|^2+\int_S|\nabla\nu|^2+\alpha\left(\sum_{i=1}^m\int_{\Omega_i}|\log J(\varphi)-\log\lambda_i|^2\right) \tag{4.11}$$

subject to (1) $\varphi(p_i)=q_i$ for $i=1,2,...,n$; (2) $||\nu||_\infty<1$ and (3) $\nu=\mu(\varphi)$.

We consider the following simplified model of the original variational problem (4.9):

$$\begin{aligned}\underset{\nu:S\to\mathbb{C},\varphi:S\to D}{\text{minimize}}\quad & \widetilde{E}^{split}(\nu,\varphi):=\int_S|\nu|^2+\int_S|\nabla\nu|^2+\alpha\left(\sum_{i=1}^m\int_{\Omega_i}|\log J(\varphi)-\log\lambda_i|^2\right)\\ & \qquad+\gamma\int_S|\nu-\mu(\varphi)|^2\\ \text{subject to}\quad & (1)\ \varphi(p_i)=q_i,\ i=1,\dots,n\\ & (2)\ \|\nu\|_\infty<1.\end{aligned} \tag{4.12}$$

The last term aims to enforce the constraint (3) of the original problem (4.11) as much as possible. γ is the penalty parameter. When γ is large enough, the constraint (3) can be well satisfied. We minimize the simplified model (4.12) alternatively. That is, we minimize the model with respect to ν and φ alternatively. This will be explained in more details in the next subsection.

Similarly, the soft landmark constraint model (4.10) can also be simplified as follows by minimizing:

$$\begin{aligned}\widetilde{E}^{split}_{soft}(\nu,\varphi)=&\int_S|\nu|^2+\int_S|\nabla\nu|^2+\alpha\left(\sum_{i=1}^m\int_{\Omega_i}|\log J(\varphi)-\log\lambda_i|^2\right)+\beta\sum_{i=1}^n|\varphi(p_i)-q_i|^2\\ &+\gamma\int_S|\nu-\mu(\varphi)|^2\end{aligned} \tag{4.13}$$

subject to the constraint that $\|\nu\|_\infty<1$.

4.3. Minimization of the energy model. In this subsection, we describe how we minimize the energy models (4.12).

To simplify the problem, the surface S is firstly parameterized onto D globally using a conformal map $\phi:S\to D$. The parameterization is further adjusted by composing it with a map $f:D\to D$, such that the overall parameterization follows the prescribed area distribution while minimizing the conformality distortion. As a result, our problem is now reduced to a 2D problem to look for an optimal map $f:D\to D$ such that the composition map $\varphi:=f\circ\phi$ is our desired parameterization.

We first consider the minimization problem (4.12). Let $\tilde{\Omega}_i=\phi(\Omega_i)$. With the parameterization as introduced above, our optimization problem can be formulated as:

$$\underset{\nu:D\to\mathbb{C},f:D\to D}{\text{minimize}}\quad \widetilde{E}^{split}(\nu,f):=\int_D|\nu|^2+\int_D|\nabla\nu|^2+\alpha\left(\sum_{i=1}^m\int_{\tilde{\Omega}_i}|\log J(f)-\log\lambda_i|^2\right)$$

$$+\gamma\int_D |\nu-\mu(f)|^2$$

$$\text{subject to} \quad (1)\ f\circ\phi(p_i)=q_i,\ i=1,\dots,n$$
$$(2)\ \|\nu\|_\infty<1. \tag{4.14}$$

Under this setting, the area distribution λ_i is now defined on $\tilde{\Omega}_i$, which should be adjusted based on the conformal factor of ϕ to compensate for the area distortion introduced by ϕ.

Conventional penalty method increases the penalty parameter γ in each iteration until ∞. To further improve the efficiency of the algorithm, we fix the penalty parameter γ to be a large enough constant and solve only one optimization problem.

Suppose we are in the n^{th} iteration with (ν_n, f_n), we first consider the derivative of the area mismatching term $E_{area}(f)=\int_\Omega|\log J(f)-\log\lambda|^2$. Here, we simplify our discussion by considering the area mismatching on Ω only.

Now we wish to find a vector field v to perturb f_n, so that the area mismatching term $E(f+\epsilon v)$ decreases for some small value of ϵ. More precisely, we wish to find the first variation of $E(f_n)$ such that $E(f_n+\epsilon v)$ decreases most rapidly. The desired direction is simply the negative of the functional derivative. Consider

$$\begin{aligned}
&\frac{d}{d\epsilon}E_{area}(f_n+\epsilon v)\Big|_{\epsilon=0}\\
=&\int_\Omega\frac{\partial}{\partial\epsilon}\left(|\log J(f_n+\epsilon v)-\log\lambda|^2\right)\Big|_{\epsilon=0}\\
=&\int_\Omega\frac{2}{J(f_n+\epsilon v)}\left(\log J(f_n+\epsilon v)-\log\lambda\right)\frac{d}{d\epsilon}J(f_n+\epsilon v)\Big|_{\epsilon=0}\\
=&\int_\Omega\frac{4}{J(f_n)}(\log J(f_n)-\log\lambda)\left(\frac{\partial f_n^1}{\partial x}\frac{\partial v_2}{\partial y}+\frac{\partial f_n^2}{\partial y}\frac{\partial v_1}{\partial x}-\frac{\partial f_n^1}{\partial y}\frac{\partial v_2}{\partial x}-\frac{\partial f_n^2}{\partial x}\frac{\partial v_1}{\partial y}\right),
\end{aligned}$$

where $f_n=(f_n^1,f_n^2):\mathbb{R}^2\to\mathbb{R}^2$ and $v=(v_1,v_2):\mathbb{R}^2\to\mathbb{R}^2$. By using integration by parts, we have

$$\begin{aligned}
&<\nabla E_{area}(f_n),v>\\
=&\frac{d}{d\epsilon}E_{area}(f_n+\epsilon v)\Big|_{\epsilon=0}\\
=&\int_\Omega\left[\frac{\partial}{\partial x}\left(\frac{4}{J(f_n)}(\log J(f_n)-\log\lambda)\frac{\partial f_n^2}{\partial y}\right)-\frac{\partial}{\partial y}\left(\frac{4}{J(f_n)}(\log J(f_n)-\log\lambda)\frac{\partial f_n^2}{\partial x}\right)\right]v_1\\
&+\left[\frac{\partial}{\partial y}\left(\frac{4}{J(f_n)}(\log J(f_n)-\log\lambda)\frac{\partial f_n^1}{\partial x}\right)-\frac{\partial}{\partial x}\left(\frac{4}{J(f_n)}(\log J(f_n)-\log\lambda)\frac{\partial f_n^1}{\partial y}\right)\right]v_2.
\end{aligned}$$

Therefore, the functional derivative ∇E is obtained. By taking the negative of ∇E, we have the descent direction:

$$df_n=-\begin{pmatrix}\frac{\partial}{\partial x}\left(\frac{4}{J(f_n)}(\log J(f_n)-\log\lambda)\frac{\partial f_n^2}{\partial y}\right)-\frac{\partial}{\partial y}\left(\frac{4}{J(f_n)}(\log J(f_n)-\log\lambda)\frac{\partial f_n^2}{\partial x}\right)\\ \frac{\partial}{\partial y}\left(\frac{4}{J(f_n)}(\log J(f_n)-\log\lambda)\frac{\partial f_n^1}{\partial x}\right)-\frac{\partial}{\partial x}\left(\frac{4}{J(f_n)}(\log J(f_n)-\log\lambda)\frac{\partial f_n^1}{\partial y}\right)\end{pmatrix}. \tag{4.15}$$

Once we have found df_n, the mapping is updated to $f_n+\kappa df_n$ for some step-size κ. Determining a suitable step-size is important for the minimization process, which will be discussed in Section 5.3.

As the mapping is perturbed from f_n to $f_n+\kappa df_n$, its associated Beltrami coefficient is also purturbed. From the Beltrami equation, the pertubation μ_{df_n} of the Beltrami coefficient can be explicitly computed. Note that

$$\frac{\partial(f_n+\kappa df_n)}{\partial\bar{z}}=(\mu(f_n)+\mu_{df_n})\frac{\partial(f_n+\kappa df_n)}{\partial z}. \tag{4.16}$$

By a simple calculation, we obtain

$$\mu_{df_n}=\kappa\left(\frac{\partial df_n}{\partial\bar{z}}-\mu(f_n)\frac{\partial df_n}{\partial z}\right)\Big/\frac{\partial(f_n+\kappa df_n)}{\partial z}. \tag{4.17}$$

From above, we transform the displacement df_n of the mapping f_n to the variation of the Beltrami coefficient μ_{df_n}. Similarly, we can compute the decent direction for the energy term $\int_D|\nu_n-\mu(f_n)|^2$, which is given by

$$d\mu_p=2(\nu_n-\mu(f_n)). \tag{4.18}$$

Therefore, the decent direction for the energy term

$$\alpha\left(\sum_{i=1}^{m}\int_{\tilde{\Omega}_i}|\log J(f_n)-\log\lambda_i|^2\right)+\gamma\int_D|\nu_n-\mu(f_n)|^2$$

is given by $d\mu=\alpha\mu_{df_n}+\gamma d\mu_p$. We then update μ_n to $\tilde{\mu}=\mu_n+td\mu$ for some small step-size t.

To sum up, the above discussion tells us how to update the Beltrami coefficient so as to minimize:

$$\alpha\left(\sum_{i=1}^{m}\int_{\tilde{\Omega}_i}|\log J(f_n)-\log\lambda_i|^2\right)+\gamma\int_D|\nu_n-\mu(f_n)|^2. \tag{4.19}$$

We can then solve the Beltrami equation with $\tilde{\mu}$ as the Beltrami coefficient, while enforcing the landmark constraints $f\circ\phi(p_i)=q_i$, $i=1,2,\ldots,n$. We then obtain the corresponding mapping $\tilde{f}$, whose Beltrami coefficient closely resembles to $\tilde{\mu}$. Note that this mapping satisfies the hard landmark constraints. Since $\tilde{\mu}$ may not be admissible with the landmark constraints enforced, the Beltrami coefficient of $\tilde{f}$ may not be exactly equal to $\tilde{\mu}$. We set $\mu_{n+1}=\mu(\tilde{f})$.

In this paper, we solve the Beltrami equation using the *Linear Beltrami Solver (LBS)* as introduced in [19]. We will now describe LBS briefly. In fact, the Beltrami equation can be reduced to two elliptic PDEs. We write $f=u+\sqrt{-1}v$. From the Beltrami Equation (3.1),

$$\mu=\frac{(u_x-v_y)+\sqrt{-1}\,(v_x+u_y)}{(u_x+v_y)+\sqrt{-1}(v_x-u_y)}. \tag{4.20}$$

Suppose $\mu=\rho+\sqrt{-1}\,\tau$. Then

$$\nabla\cdot\left(A\begin{pmatrix}u_x\\u_y\end{pmatrix}\right)=0\quad\text{and}\quad\nabla\cdot\left(A\begin{pmatrix}v_x\\v_y\end{pmatrix}\right)=0. \tag{4.21}$$

Here, $A=\begin{pmatrix}\alpha_1&\alpha_2\\\alpha_2&\alpha_3\end{pmatrix}$ is symmetric positive definite where $\alpha_1=\frac{(\rho-1)^2+\tau^2}{1-\rho^2-\tau^2}$; $\alpha_2=-\frac{2\tau}{1-\rho^2-\tau^2}$ and $\alpha_3=\frac{1+2\rho+\rho^2+\tau^2}{1-\rho^2-\tau^2}$.

Hence, given μ, the quasi-conformal map f can be reconstructed by solving equations (4.21) subject to the landmark constraints. In the discrete case, the elliptic PDEs (4.21) can be discretized as two linear systems subject to the landmark constraints. Such a solver for quasi-conformal map is called the *Linear Beltrami Solver (LBS)*. For details, please refer to [19].

With the new Beltrami coefficient μ_{n+1}, our next step is to minimize the energy terms

$$\widehat{E}(\nu) := \int_D |\nu|^2 + \int_D |\nabla \nu|^2 + \gamma \int_D |\nu - \mu_{n+1}|^2 \tag{4.22}$$

with respect to ν. Note that these terms act as the regularizer of the energy model as well as minimizing the Beltrami coefficient to enforce the bijectivity constraint. By considering the Euler–Lagrange equation, the optimization problem (4.22) is equivalent to solving

$$(-\Delta + 2I + 2\gamma I)\nu = 2\gamma \mu_{n+1}. \tag{4.23}$$

By solving the Euler–Lagrange Equation (4.23), ν_{n+1} can be obtained, which minimizes the energy functional (4.22). The energy functional involves the L^2 norm of ν. We remark that minimizing the L^2 norm of ν cannot theoretically guarantee the constraint $\|\nu\|_\infty < 1$ to be satisfied. However, in our experiments, it is observed that minimizing the L^2 norm of ν is already sufficient to produce a diffeomorphic mapping (that is, $\|\nu\|_\infty < 1$), even for the case with a very large deformation. In the very extreme case with an extremely large deformation, one may minimize the L^p norm of ν with bigger p instead of the L^2 norm. However, the optimization problem can no longer be solved efficiently by solving a sparse linear system. Alternatively, a simple projection (truncation) step can also be added in the procedure to obtain a diffeomorphic mapping for the very extreme case:

$$\mathcal{P}_\delta(\nu_{n+1})(x) = \begin{cases} \nu_{n+1}(x) & \text{if } |\nu_{n+1}(x)| < 1 \\ (1-\delta)(\cos(\arg(\nu_{n+1})) + i\sin(\arg(\nu_{n+1}))) & \text{if } |\nu_{n+1}(x)| \geq 1. \end{cases} \tag{4.24}$$

In practical situations, the truncation step is never needed to ensure the bijectivity. Minimizing L^2 norm of ν already suffices to handle very large deformations. The truncation step may only be necessary when we are handling extremely large deformations. Such extreme cases are not common in practical situations.

Once ν_{n+1} is obtained, we can then update f_{n+1} by solving the Beltrami equation with $\mu = \nu_{n+1}$ using LBS. We repeat the above process until $\|\mu(f_{n+1}) - \mu(f_n)\|_\infty \leq \epsilon$ for some small threshold ϵ. The overall procedure is summarized in Algorithm 1.

4.4. Optimized parameterization of high-genus surfaces. The discussions in last subsections assume the underlying surface to be simply-connected. In fact, our proposed method can also be applied to high-genus surfaces. For high-genus surfaces, we propose to compute the optimized quasiconformal parameterization into its universal covering space, which follows the prescribed area distribution while minimizing the local geometric distortion.

Every high-genus surface S (with genus $g \geq 1$) is associated with a universal covering space $\widehat{S} \subseteq \mathbb{R}^2$. A universal covering space is a simply-connected space with a continuous surjective map $\psi : \widehat{S} \to S$ satisfying the following: for any $p \in S$, there exists an open neighborhood U of p such that $\psi^{-1}(U)$ is a disjoint union of open sets in $\widehat{S}$, in which

Algorithm 1: *Optimized conformal parameterization with controllable area distortion*

Input: Surface S and its conformal parameterization ϕ; Prescribed area distribution λ; Boundary condition for the target domain D.

Output: Optimized parameterization $f\circ\phi: S\to D$ balancing between the area distortion and conformality distortion.

Initial $\nu_0=0$; $f_0=Id$; $\mu_0=0$;
repeat
  Compute df_n minimizing the area mismatching term;
  Compute the step-size κ as described in Section 5.3;
  Compute μ_{df_n}, $d\mu_p$ and $d\mu=\alpha\mu_{df_n}+\gamma d\mu_p$. Set $\tilde{\mu}=\mu_n+td\mu$;
  Use LBS to reconstruct $\tilde{f}$ from $\tilde{\mu}$ with landmark constraints;
  Compute $\mu_{n+1}=\mu(\tilde{f})$;
  Solve ν_{n+1} from the Euler-Lagrange equation

$$(-\Delta+2I+2\gamma I)\nu=2\gamma\mu_{n+1};$$

  Update $\nu_{n+1}\leftarrow\mathcal{P}_\delta(\nu_{n+1})$ (See equation 4.24);
  Use LBS to reconstruct f_{n+1} from ν_{n+1} with landmark constraints;
  Compute $\mu(f_{n+1})$;
until $||\mu(f_{n+1})-\mu(f_n)||_\infty\le\epsilon$;

each of these disjoint open sets is mapped homeomorphically onto U by ψ. We call ψ the *covering map*. The covering map is invariant under the *deck transformation*. A deck transformation is a map $\sigma:\widehat{S}\to\widehat{S}$ such that $\psi\circ\sigma=\psi$. The collection of all deck transformations forms a group, called the *Deck transformation group*, which is $2g$ dimensional. When $g=1$, $\widehat{S}$ is equal to the whole plane $\mathbb{R}^2$. When $g>1$, $\widehat{S}$ is the *Poincarè disk* $\mathbb{H}^2$. The Poincarè disk $\mathbb{H}^2$ is a unit disk equipped with a metric defined as follows:

$$ds^2=\frac{4dzd\bar{z}}{(1-z\bar{z})^2}. \tag{4.25}$$

Let $p\in S$ be a point on S, which is called a *base point*. We consider the collection of all closed loops based at p. Two such closed loops c_1 and c_2 are said to be *equivalent* if there exists a homotopy $H:[0,1]\times[0,1]\to S$ such that $H(0,\cdot)=c_1$ and $H(1,\cdot)=c_2$. All equivalent loops form an equivalence class. The set of all equivalent classes form a group called the *fundamental group*, $\pi(S,p)$, of S. Let $\{a_1,b_1,...,a_i,b_i,...,a_g,b_g\}$ be a basis of $\pi(S,p)$. Suppose r, s are two elements of $\pi(S,p)$, which are two closed loops based at p. The product of r and s is defined as follows:

$$(rs)(t):=\begin{cases} r(2t) & 0\le t\le\frac{1}{2},\\ s(2t-1) & \frac{1}{2}\le t\le 1.\end{cases} \tag{4.26}$$

The identity element is the constant map at the base point. The inverse a_i^{-1} of a loop a_i is the same loop with opposite direction at the base point. Slicing along the basis, S becomes a simply-connected open surface, denoted by S^{cut}, which is called the *fundamental domain*. The fundamental group basis $\{a_1,b_1,a_2,b_2,...,a_g,b_g\}$ is called *canonical* if any two loops intersect only at the base point p. From algebraic topology,

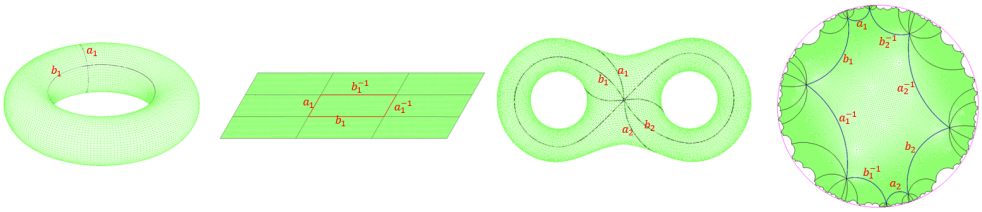

(a) *Torus and its fundamental polygon* (b) *2-Tours and its fundamental polygon*

Fig. 4.1: *Illustration of conformal embedding of high-genus surfaces into their universal covering spaces. (a) shows a genus one torus and the corresponding conformal embedding into the universal covering space (*$\mathbb{C}$*). (b) shows a genus two 2-torus and the corresponding conformal embedding into the universal covering space (Poincarè disk).*

the boundary of the fundamental domain with respect to the canonical loops is given by

$$a_1 b_1 a_1^{-1} b_1^{-1} a_2 b_2 a_2^{-1} b_2^{-1} \cdots a_g b_g a_g^{-1} b_g^{-1}. \tag{4.27}$$

Each canonical cut can be chosen to be the shortest path in its equivalence class. The fundamental domain S^{cut} can be conformally embedded onto a 2D domain $\Omega \subset \mathbb{R}^2$, called the fundamental polygon. By glueing copies of Ω together along its boundaries, the universal covering space of S, $\widehat{S}$, is obtained. As a result, we get the covering map $\psi : \widehat{S} \to S$. See Figure 4.1 for an illustration of the idea.

Now, let $\psi^{-1}(S) = \bigcup_{\alpha \in I} \widetilde{D}_\alpha$, where I is the index set. The fundamental polygon, Ω, belongs to one of the pieces, $\widetilde{D}_\alpha \subset \widehat{S}$. Two adjacent $\widetilde{D}_\alpha$ and $\widetilde{D}_\beta$ intersect at the edges if $\alpha \neq \beta$. Furthermore, we can find the generator $\{\varphi_1, \phi_1, \varphi_2, \phi_2, ..., \varphi_g, \phi_g\}$ of the Deck transformation group of S_1 such that $\varphi_i(a_i) = a_i^{-1}$ and $\phi_i(b_i) = b_i^{-1}$ $(1 \leq i \leq g)$. Here, we identify a_i and b_i with the boundaries of the fundamental polygon, which are the projected images of a_i and b_i in the universal covering space. $\{\varphi_1, \phi_1, \varphi_2, \phi_2, ..., \varphi_g, \phi_g\}$ are called the Fuchsian group generators. When $g = 1$, φ_i and ϕ_i are just translations in $\mathbb{R}^2$. When $g > 1$, φ_i and ϕ_i are Möbius transformations of the unit disk, which can be computed explicitly. We will describe the computation of φ_1. The other Fuchsian group generators can be obtained in the same way. Suppose the starting point and ending points of c_1 are r and s, and the starting point and ending points of c_1^{-1} are s' and r'. We need to look for a Möbius transformation φ_1 such that $\varphi_1(r) = r'$ and $\varphi_1(s) = s'$. We first compute a Möbius transformation to map r to the origin, which is given by: $\rho_1(z) = (z - r)/(1 - \bar{r}z)$. Then, ρ_1 maps $\overline{rs}$ to a radial Euclidean line. Let the angle between $\rho_1(\overline{rs})$ and the real axis be θ, and let $\rho_2(z) = e^{-i\theta} z$. Then, $\rho_2 \circ \rho_1$ maps r to the origin and $\overline{rs}$ to the real axis. Similarly, we can find Möbius transformation ρ_1' and ρ_2' such that $\rho_2' \circ \rho_1'$ maps r' to the origin and $\overline{r's'}$ to the real axis. The deck transformation φ_1 is then given by: $\varphi_1 = \rho_1'^{-1} \circ \rho_2'^{-1} \circ \rho_2 \circ \rho_1$.

In this work, we apply the Ricci flow method introduced by Gu et al. in [12, 32] to compute the conformal embedding of S into its universal covering space $\widehat{S}$. To obtain the optimized quasiconformal parameterization, we proceed to adjust the conformal embedding on the universal covering space. More specifically, we look for a map $\tilde{f} : \widehat{S} \to \widehat{S}$ such that $\psi \circ \tilde{f}^{-1}$ is a covering map of S. This can be done by computing a map f on one fundamental polygon $\widetilde{D}_\alpha$ that satisfies the periodic boundary constraints. The overall map $\tilde{f}$ can be obtained by the periodic extension of f. More specifically, to obtain the

optimized quasiconformal map that follows the prescribed area distribution, we propose to compute $f:\widetilde{D}_\alpha\to\widehat{S}$ that optimizes Model 4.12 subject to the boundary constraints that

$$\varphi_i(f(a_i))=f(a_i^{-1}) \text{ and } \phi_i(f(b_i))=f(b_i^{-1}). \tag{4.28}$$

The above optimization problem can be solved similarly as described in the last subsection with the addition of the periodic boundary constraints.

5. Numerical implementation

In this section, we discuss the numerical implementation of our proposed algorithm in detail.

5.1. Assignment of λ_i. In our model (4.12), the area distribution function λ_i associated to the subdomains $\tilde{\Omega}_i=\phi(\Omega_i)$ are prescribed by users, where ϕ is a conformal parameterization of S. In practice, the subdomains are prescribed according to users' preference on which regions to be enlarged, squeezed or area preserving. In the discrete case, $\tilde{\Omega}_i$ can be considered as a union of triangular faces.

Now, the area distribution function λ_i is a scalar function defined on each triangular faces of $\tilde{\Omega}_i$, which is prescribed by users according to their applications. For the purpose of illustration, we consider a simple case. The more complicated case can be handled similarly. Suppose we aim to obtain an optimal parameterization φ of the surface S onto the parameter domain D, which minimizes conformality and area distortions. In this case, we set $\tilde{\Omega}_i=D$. Without loss of generality, we may assume that D is rescaled such that the area of S and D are equal. Our goal is to find a homeomorphism $f:D\to D$ such that $\varphi=f\circ\phi$ is our desired optimal parameterization. Note that the discrete Jacobian of the mapping f on each triangular face T of D is simply the ratio between the area of T and $f(T)$.

Our proposed model minimizes the area distortion by minimizing an area distortion term $\int_\Omega|\log J(f)-\log\lambda_i|^2$. In order to obtain a parameterization φ of S that preserves area as good as possible, we set

$$\lambda(T)=\frac{\mathcal{A}(\phi^{-1}(T))}{\mathcal{A}(T)},$$

where $\mathcal{A}(\phi^{-1}(T))$ and $\mathcal{A}(T)$ denotes the area of $\phi^{-1}(T)$ and T respectively.

On the other hand, if we need to enlarge or squeeze some subdomain $\tilde{\Omega}_i\subset D$ by a ratio of $k\in\mathbb{R}^+$, we can set $\lambda(T)=\frac{k\mathcal{A}(\phi^{-1}(T))}{\mathcal{A}(T)}$ for all $T\subset\Omega_i$. The area of D should be suitably rescaled such that equation (4.3) is satisfied.

5.2. Discrete differential operators. Consider a triangle $T=[v_1,v_2,v_3]$ where $v_k=x_k+iy_k$ for $k=1,2,3$. Suppose we have a function f on the triangle. By the first order approximation

$$f(z+p)\approx f(p)+f_z(p)z+f_{\bar{z}}(p)\bar{z}, \tag{5.1}$$

we have the following equality on each triangle in the triangulation mesh:

$$\begin{pmatrix} f(v_1)\\ f(v_2)\\ f(v_3)\end{pmatrix}=\begin{pmatrix} v_1 & \overline{v_1} & 1\\ v_2 & \overline{v_2} & 1\\ v_3 & \overline{v_3} & 1\end{pmatrix}\begin{pmatrix} f_z(p)\\ f_{\bar{z}}(p)\\ f(p)\end{pmatrix}, \tag{5.2}$$

where p is any interior point in the triangle. By solving this equation on each triangle, we can define the discrete differential operator D_z and $D_{\bar{z}}$ explicitly. With the discrete differential operator D_z and $D_{\bar{z}}$, we can obtain the discrete Beltrami coefficients directly.

Let $T_1 = [v_i, v_j, v_k]$ and $T_2 = [v_i, v_j, v_l]$. The mesh Laplacian is defined as:

$$\Delta(f(v_i)) = \sum_{T \in N_i} \frac{\cot \alpha_{ij} + \cot \beta_{ij}}{2} (f(v_j) - f(v_i)), \tag{5.3}$$

where α_{ij} and β_{ij} are the two interior angles of T_1 and T_2 which are opposite to the edge $[v_i, v_j]$ [11].

5.3. Descent direction for the area mismatching term. Recall that the descent direction of the area mismatching term in equation (4.15):

$$df_n = -\begin{pmatrix} \frac{\partial}{\partial x}\left(\frac{4}{J(f_n)}(\log J(f_n) - \log\lambda)\frac{\partial f_n^2}{\partial y}\right) - \frac{\partial}{\partial y}\left(\frac{4}{J(f_n)}(\log J(f_n) - \log\lambda)\frac{\partial f_n^2}{\partial x}\right) \\ \frac{\partial}{\partial y}\left(\frac{4}{J(f_n)}(\log J(f_n) - \log\lambda)\frac{\partial f_n^1}{\partial x}\right) - \frac{\partial}{\partial x}\left(\frac{4}{J(f_n)}(\log J(f_n) - \log\lambda)\frac{\partial f_n^1}{\partial y}\right) \end{pmatrix},$$

or in the complex form:

$$\begin{aligned} df_n = &-\left(\frac{\partial}{\partial \bar{z}}\right)\left(\frac{8}{J(f_n)}(\log J(f_n) - \log\lambda)\frac{\partial f_n}{\partial z}\right) \\ &+\left(\frac{\partial}{\partial z}\right)\left(\frac{8}{J(f_n)}(\log J(f_n) - \log\lambda)\frac{\partial f_n}{\partial \bar{z}}\right) \end{aligned}$$

where $f_n = f_n^1 + i f_n^2$. By the discretization of the differential operator introduced in section 5.1, we have the discrete version of the descent direction:

$$df_n = -D_z^*(M D_z f_n) + D_{\bar{z}}^*(M D_{\bar{z}} f_n), \tag{5.4}$$

where M is a diagonal matrix with elements $\frac{8}{J(f_n)}(\log J(f_n) - \log\lambda)$ defined on each triangle of the mesh and D^* is the conjugate transpose of a matrix D.

5.4. Choice of the parameter. After the decent direction df reducing the area mismatching energy term is found, we also need to choose the step-size κ. Let $v_i = [x_i, y_i]$ and $df(v_i) = [dx_i, dy_i]$, where $v_i \in [v_1, v_2, v_3]^T = \mathcal{T}$ are the vertices of a triangle $\mathcal{T}$. κ is chosen as follows: To solve the optimization problem in Algorithm 2, we first denote

Algorithm 2: *Step-size* κ

Input: Triangular mesh with vertex v; Descent direction df.

1 Initial $\kappa = 1$;
2 **repeat**
3 Find κ^* such that $\kappa^* =$

$$\max_{0<\kappa\le 1}\left\{\kappa : \det\begin{pmatrix} x_1+\kappa dx_1 & x_2+\kappa dx_2 & x_3+\kappa dx_3 \\ y_1+\kappa dy_1 & y_2+\kappa dy_2 & y_3+\kappa dy_3 \\ 1 & 1 & 1 \end{pmatrix} > 0,\ \mathcal{T} = [v_1, v_2, v_3]^T\right\}.$$

4 $df \leftarrow k^* df$;
5 $\kappa \leftarrow \kappa^*$.
6 **until** $\kappa < 1$;

$x_{ij} = x_i - x_j$ for simplicity. Then we can rewrite the determinant as

$$\det\left[\begin{pmatrix} x_1 & x_2 & x_3 \\ y_1 & y_2 & y_3 \\ 1 & 1 & 1 \end{pmatrix} + \kappa \begin{pmatrix} dx_1 & dx_2 & dx_3 \\ dy_1 & dy_2 & dy_3 \\ 0 & 0 & 0 \end{pmatrix}\right] = A\kappa^2 + B\kappa + C,$$

where

$$\begin{aligned} A &= dx_{21}dy_{31} - dx_{31}dy_{21}, \\ B &= dx_{21}y_{31} + dy_{31}x_{21} - dx_{31}y_{21} - dy_{21}x_{31}, \\ C &= x_{21}y_{31} - x_{31}y_{21}. \end{aligned}$$

Therefore, by considering the above quadratic equation, we can determine the condition on κ that guarantees the preservation of the orientation for each triangle, i.e. avoiding flips of triangles on the mesh.

5.5. Initial parameterization. As we can see that the proposed energy model (4.14) is non-convex, finding an appropriate initial parameterization is important. In Algorithm 1, we choose the conformal parameterization as the initial parameterization if there is no landmark constraint. However, if landmark constraints are enforced, we set the initial parameterization to be a minimizer of the energy model (4.14) with $\alpha = 0$. This initialization gives us an optimized conformal parameterization, which satisfies the prescribed landmark constraints.

6. Experimental results

We have tested our proposed algorithm on both synthetic and real data. In this section, experimental results will be shown. We set the parameter $\gamma = 1$ in each example.

6.1. Synthetic examples.

Example 1. We first test our proposed model on a synthetic example, whose area distribution is prescribed in such a way that the central region of the rectangular mesh is expanded. In this example, the regularization terms in our model

$$\int_D |\nu|^2 + |\nabla\nu|^2$$

are removed. The aim is to check the effectiveness of the area mismatching term to enforce the prescribed area distribution.

To prescribe the area distribution, we take an initial mesh and deform it to obtain the area distortion under the deformation. Figure 6.1(a) shows the initial mesh of a 2D rectangular mesh. It is deformed in such a way that the central region is enlarged, which is shown in (b). (c) shows the logarithm of the Jacobian determinant $\log\lambda$ of the deformation, visualized by a colormap. $\log\lambda$ is used to define the area distribution in this example. More specifically, we set the subdomain to be the whole rectangular mesh and use $\log\lambda$ as our target area distribution. Our goal is to obtain a deformation using our proposed algorithm, which follows the prescribed area distribution as good as possible.

Figure 6.2(a) shows the result obtained by our proposed algorithm. The colormap describes the area mismatching $\log J(f) - \log\lambda$. The area distortion is close to 0 over the whole domain, indicating that the area distribution perfectly matches with the prescribed one. Although the area distribution can be matched accurately, conformality distortion is large, especially on the region near the boundary of the ball. Figure 6.2(b)

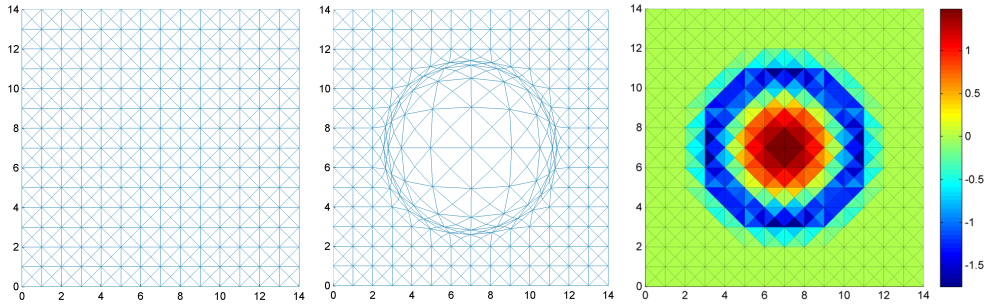

Fig. 6.1: *Setup in Example 1. (a) shows the original mesh S, which is a 2D square domain. The original mesh S is deformed, under which the central disk is enlarged, as shown in (b). (c) shows the logarithm of the Jacobian determinant of the deformation, visualized by a colormap. It is used to define the area distribution in Example 1.*

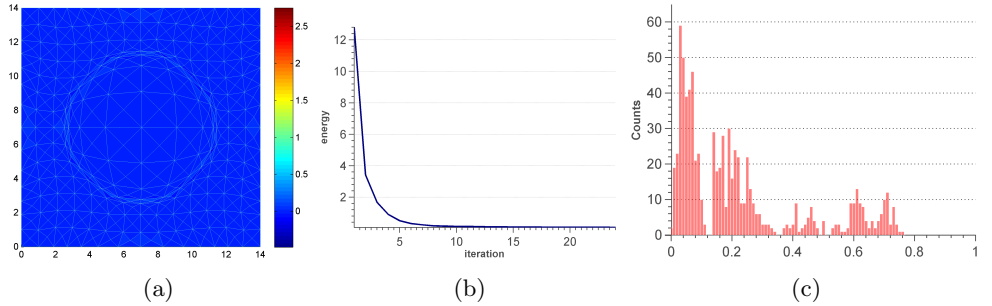

Fig. 6.2: *Result of Example 1 without considering the regularization terms. (a) shows the optimized parameterization that matches the prescribed area distribution. (b) shows the plot of energy versus iterations in the algorithm. (c) shows the histogram of magnitude of the Beltrami coefficient, which describes the distribution of the conformality distortion under the optimized parameterization.*

shows the energy versus iterations in the algorithm. Since regularization terms are not considered, a zero energy means an exact matching of the area distribution. (c) shows the distribution of the conformality distortion. Note that the regularization terms are removed and hence the conformality distortion of the parameterization is not under control. Some triangles have large Beltrami coefficients with $|\mu| > 0.75$ (on the boundary of the expanding region), which indicate large conformality distortions.

Example 2. In the second example, we add the regularization term into the model. The coefficient α associated to the area distortion term is set to be $\alpha = 0.3$. Figure 6.3 shows the obtained deformation. As the regularization term is added, the area distribution cannot match the prescribed one perfectly, which is as shown in Figure 6.3(a). On the other hand, the regularization terms prevent the triangles on the boundary of expanding region from being squeezed (compared with Example 1). As shown in 6.3(a), the area mismatching $\log J(f) - \log \lambda$ is relatively bigger near the boundary of the expanding region. Furthermore, the minimization of the L^2-norm of μ reduces the

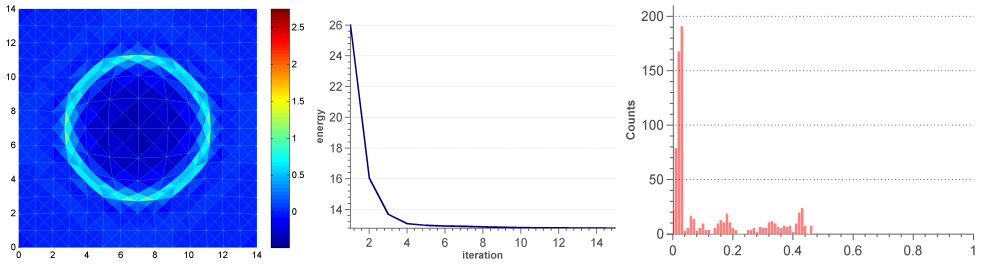

(a) (b) (c)

Fig. 6.3: *Results of Example 2. (a) shows the optimized parameterization in Example 2, in which the regularization terms are included in the model with* $\alpha = 0.3$. *(b) shows the plot of energy versus iterations in the algorithm. (c) shows the histogram of magnitude of the Beltrami coefficient, which describes the distribution of the conformality distortion under the optimized parameterization.*

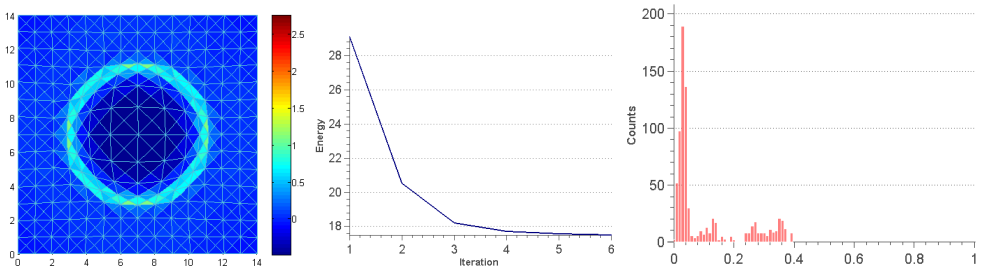

(a) (b) (c)

Fig. 6.4: *Results of Example 3. (a) shows the optimized parameterization in Example 2, in which the regularization terms are included in the model with* $\alpha = 0.1$. *(b) shows the plot of energy versus iterations in the algorithm. (c) shows the histogram of magnitude of the Beltrami coefficient, which describes the distribution of the conformality distortion under the optimized parameterization.*

conformality distortion of the deformation. As shown in Figure 6.3(c), the conformality distortion $|\mu|$, is smaller (with $\|\mu\|_\infty = 0.4609$), when comparing with Example 1. It means the obtained deformation preserves more conformality.

Example 3. In this example, we test the same set-up as in Example 2 with $\alpha = 0.1$. By reducing α, we tolerate for the area mismatching in order to preserve more conformality. As shown in Figure 6.4(c), the overall conformality distortion of the obtained deformation is less than those in Example 1 and Example 2. However, the area mismatching is larger, when compared with Example 1 and 2. These examples demonstrate that there is always a balance between the area distortion and conformality distortion of a parameterization. The parameter α is therefore a convenient tool to control the balance.

Example 4. In this example, we define the area distribution λ, which is compactly supported and satisfies $\log\lambda = 2$ in a small region $\tilde{\Omega}$ (the red region in Figure 6.5(a)). The colormap on Figure 6.5(a) is given by $\log\lambda$. In other words, we aim to obtain a transformation, which enlarges the area of the (red) interested region. We set $\alpha = 10/3$

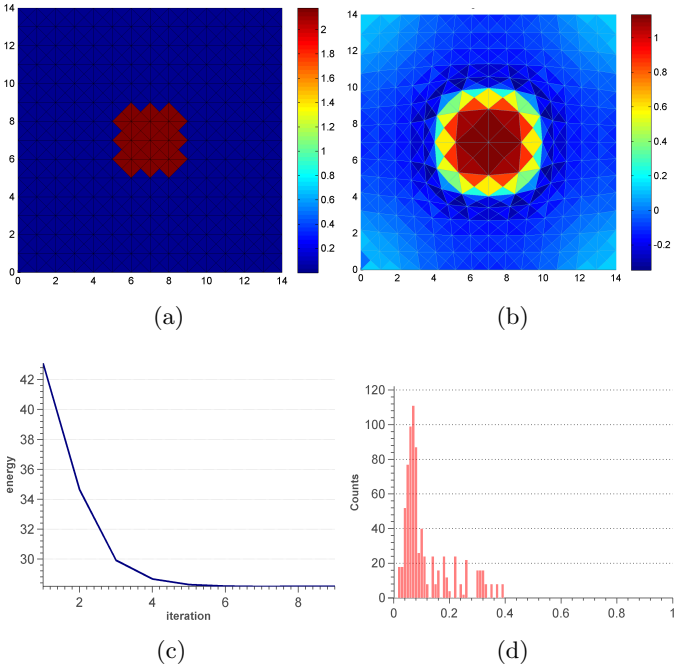

Fig. 6.5: *Results of Example 4. S is again chosen as the square mesh. (a) shows the prescribed area distribution* $\log\lambda$*, which is compactly supported in the red region. (b) shows the optimized parameterization obtained from our algorithm. The colormap is given by the logarithmic of the Jacobian determinant of the parameterization. (c) shows the plot of energy versus iterations in the algorithm. (d) shows the histogram of the magnitude of the Beltrami coefficient.*

to balance between area and conformality distortions of the parameterization. (b) shows the obtained transformation f, whose colormap is given by $\log J(f)$. As expected, the red region is enlarged under the transformation. Note that $\log J(f)$ is not exactly equal to the prescribed area distribution $\log\lambda$, as a non-zero α is set to balance between the conformality distortion and area mismatching. (c) shows the plot of the energy versus iterations. Note that the energy is minimized iteratively. (d) shows the histogram of $|\mu|$ asssociated to the obtained transformation, which measures the conformality distortion.

Example 5. In this example, we test our proposed model with landmark constraints. In Figure 6.6(a), two dots in red color show the initial positions $\{p_1,p_2\}$ of two landmark points. Their target positions $\{q_1,q_2\}$ are given by two blue dots. We aim to compute a landmark-aligned transformation that matches the prescribed area distribution, while minimizing the conformality distortion. In this example, we set $\tilde{\Omega}$ to be the whole domain and $\lambda=1$ on $\tilde{\Omega}$. In other words, we aim to compute a landmark-aligned transformation of the 2D rectangle, which minimizes the local geometric distortion while preserving the area as much as possible.

Figure 6.6 (b) shows the obtained transformation f with $\alpha=0$. In other words, the area mismatching term is removed in our model. Here, the colormap is given by $\log J(f)$. From the colormap, it can be observed that triangular faces in the middle (deep blue) region are squeezed drastically. It is expected since area mismatching term is not

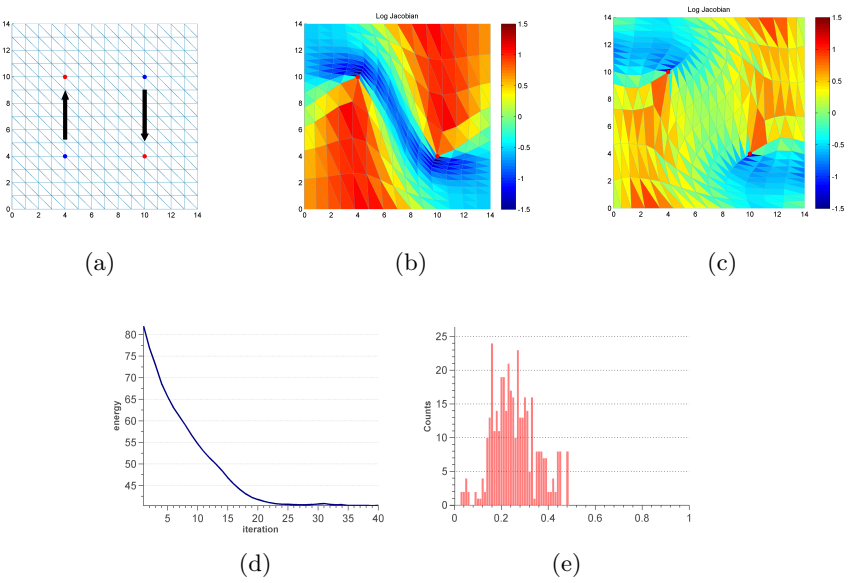

Fig. 6.6: *Results of Example 5. (a) shows the original domain S and the landmark points denoted by blue dots. Their target positions are denoted by red dots. (b) shows the landmark-aligned optimized parameterization with $\alpha=0$. The colormap is given by the logarithmic Jacobian determinant of the parameterization. (c) shows the landmark-aligned optimized parameterization with $\alpha=1$. The colormap is given by the logarithmic Jacobian determinant of the parameterization. (d) shows the plot of energy versus iterations and (e) shows the conformality distortion of the parameterization.*

included in the model. (c) shows the obtained transformation when $\alpha=1$. As the area mismatching term is included, the squeezing effect of triangular faces are eliminated. (d) shows the energy plot versus iterations and (e) shows the histogram of $|\mu|$ asssociated to the obtained transformation, which measures the conformality distortion.

Example 6. In this example, we test our proposed model on a curvilinear surface S embedded in $\mathbb{R}^3$. Let $\tilde{\Omega}$ be the whole domain $D=\phi(S)$, where ϕ is the conformal parameterization of S. As discussed in Section 5.1, we set λ to be

$$\lambda(T)=\frac{\mathcal{A}(\phi^{-1}(T))}{\mathcal{A}(T)},\forall\ T\subset\tilde{\Omega}.$$

Furthermore, we set $\alpha=1$ in this example. We apply our algorithm to compute a texture map for projecting a texture image onto the surface. Figure 6.7(a) shows the curvilinear surface and texture image used in this example. Using our proposed method, we compute an optimized parameterization of S onto the 2D texture image, which minimizes the conformality distortion and area distortion.

We first conformally parameterize S onto the 2D domain and project the texture image onto S. The result is shown in Figure 6.7(b). Under the conformal parameterization, the local geometry (conformality) is preserved, although the area can be severely distorted. Observe that the characters "8" and "5" are enlarged and distorted unnaturally at the bumps. Using our algorithm, we compute the optimized conformal parameterization minimizing the area distortion, which is shown in Figure 6.7(c). The colormap is given by the area mismatching. Note that the area mismatching are close to

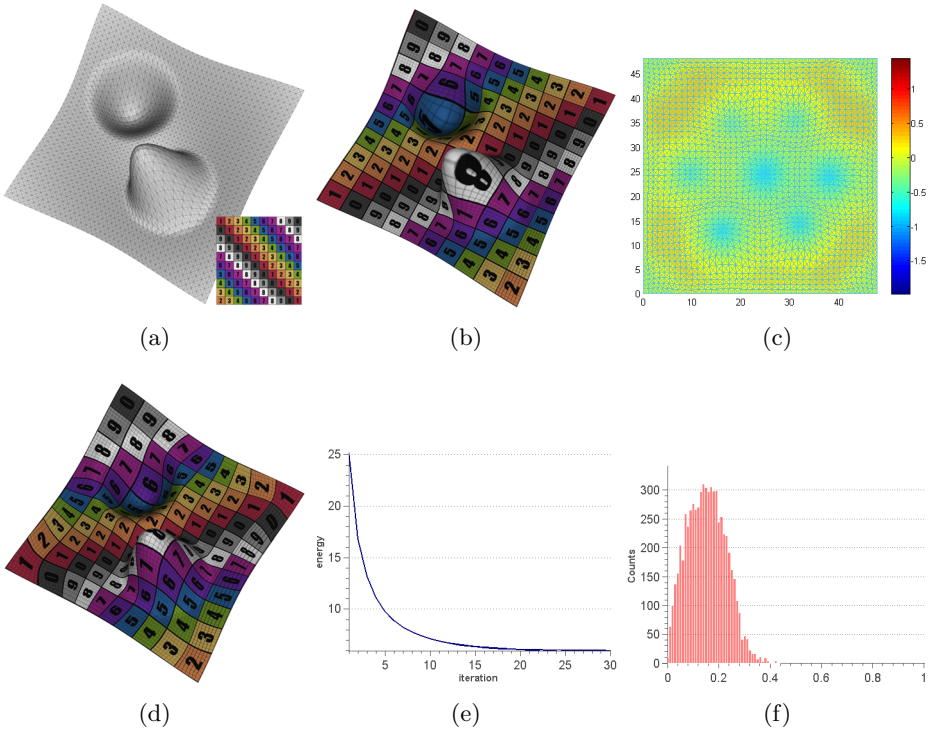

Fig. 6.7: *(a) shows a surface mesh S and the texture image. (b) shows the textured surface using the conformal parameterization. (c) shows the optimized conformal parameterization that minimizes area and conformality distortions. (d) shows the textured surface using the optimized parameterization. (e) shows the plot of energy versus iterations. (f) shows the conformality distortion of the parameterization.*

zero, meaning that the area distortion under the parameterization is small. (d) shows the textured surface using the obtained optimized parameterization. Distortions of the characters "8" and "5" at the bumps are avoided. (e) and (f) shows the energy versus iterations and the conformality distortion of the optimized parameterization respectively.

6.2. Real examples. In this subsection, we show experimental results of our proposed model on real data.

Brain surface parameterization. The complicated structure of the brain hinders the shape analysis of brain cortical surfaces. To alleviate this issue, parameterization techniques are often used to flatten the cortical surface, so that the analysis and computation can be carried out on the 2D domain. Conformal parameterizations have been widely used since they preserve the local geometry well. Hence, local geometric structures of the brain cortical surface can be visualized and scientific computing can be carried out on the 2D domain. However, the major drawback of conformal parameterizations is that they often introduce area distortion, such as a serious squeezing. This causes difficulties for the visualization of the geometric structure of the brain as well as the scientific computing on the parameter domain. Using our proposed algorithm,

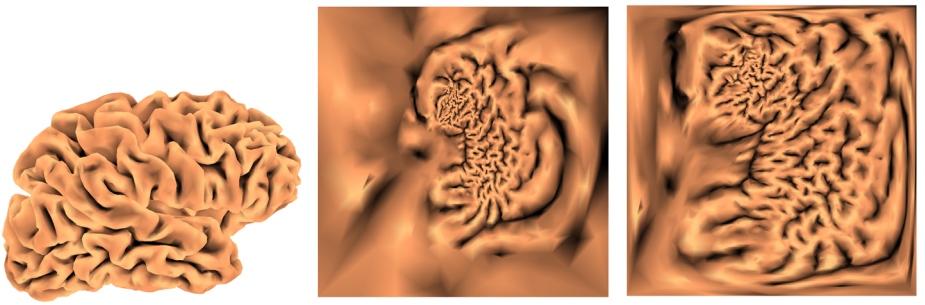

(a) (b) (c)

Fig. 6.8: *(a) shows the brain cortical surface. The colormap is given by the mean curvature of the brain surface. (b) shows the conformal parameterization. (c) shows the optimized parameterization, which minimizes both the area and conformality distortions.*

we can obtain an optimized parameterization that balances between conformality and area distortions. In particular, we set $\tilde{\Omega}$ to be the whole parameter domain and define $\lambda = 1$ on $\tilde{\Omega}$. In this example, we set $\gamma = 0.1$. Figure 6.8(a) shows a human brain cortical surface. Its conformal parameterization is shown in (b). It can be observed that a large portion of the surface are squeezed to the central region of the parameter domain under the parameterization. (c) shows the optimized parameterization obtained by our method. The squeezing effect on the parameter domain is avoided, while the geometric pattern of the sulci can be well observed.

Optimized parameterization of real 3D scanned surface. We also test our proposed algorithm on real 3D scanned surfaces embedded in $\mathbb{R}^3$. In this example, we parameterize a lion head surface with the prescribed area distribution, so that the interested part of the surface is enlarged on the parameter domain. The lion head surface is shown in Figure 6.9(a). The area distribution is defined such that the mouth and eyes of the lion head are enlarged on the parameter domain. (b) shows the conformal parameterization of the lion head surface, whose colormap is given by the prescribed area distribution $\log \lambda$. (c) shows the conformal parameterization of the lion head, whose colormap is given by the mean curvature of the surface. (d) shows the optimized parameterization obtained using our algorithm. Using our proposed algorithm with the prescribed area distribution, we successfully enlarge the mouth and eyes on the parameter domain. The result is shown in Figure 6.9(d). The shapes of the mouth and eyes are also well preserved on the parameter domain.

Vertebra bone registration. An important application of parameterizations is to compute surface registrations. Once the landmark-aligned parameterizations of two surfaces are obtained, a landmark-matching registration between the two surfaces can be easily obtained through the composition map of the parameterizations. Our proposed algorithm can also be applied to high-genus surfaces. In this example, we tested our model to register genus-one surfaces with prescribed landmark constraints. Figure 6.10 (a) shows the surface mesh of vertebra bone A. Feature landmarks are labeled as blue dots. Its conformal parameterization onto the universal covering space is shown in (b). The corresponding locations of the feature landmarks on the parameter domain are also labelled by the blue dots. In this example, we apply the algorithm in [12] to compute

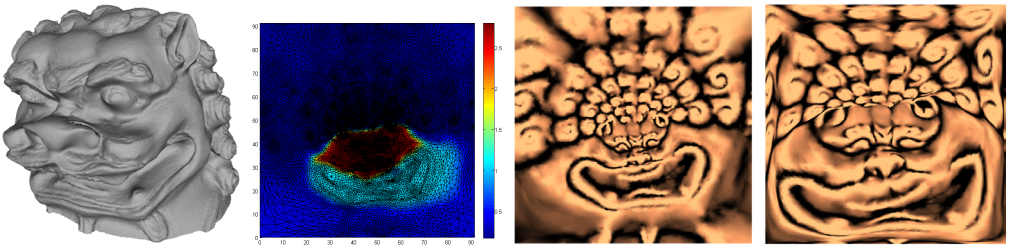

(a) (b) (c) (d)

Fig. 6.9: *(a) shows the surface mesh of a lion head. (b) shows the prescribed area distribution* $\log\lambda$*, shown on the conformal parameter domain. (c) shows the conformal parameterization. (d) shows the optimized parameterization obtained from our proposed model.*

the conformal parameterization into the universal covering space. Periodic boundary conditions are enforced. Figure 6.10(c) and (d) show the surface mesh of vertebra bone B and its conformal parameterization respectively. The red dots in (c) and (d) are the positions of the feature landmarks on the vertebra bone and its conformal parameter domain respectively. To register bone A to bone B, we parameterize bone A such that its feature landmarks are mapped to the landmark positions of bone B on its parameter domain. Our goal is to obtain a landmark-aligned parameterization, which minimizes area and conformality distortions. In this case, we set $\tilde{\Omega}$ to be the whole parameterized domain (which is the fundamental polygon in this example) and set $\lambda = 1$ on $\tilde{\Omega}$. (e) shows the optimized parameterization result of bone A. The boundaries of the fundamental polygon is allowed to move freely, which satisfy the periodic boundary constraints. Using the composition map of the parameterizations, we deform bone A to bone B, which is shown in (f). This gives the surface registration f between the two surface meshes. (g) shows the histogram of $\log J(f)$. The distribution is accumulated at zero, indicating that the obtained registration preserves the area well.

Visualization of surface-based protein. In this example, we apply our method to parameterize protein surfaces for the visualization of protein structures. Studying the surface of a protein is useful as the 3 dimensional structures of proteins can give useful information to determine their functionalities, through the comparison with other well-studied proteins. In particular, the electrostatic surface of a protein provides important information to study the protein-protein interaction [28]. In this example, the protein data are obtained from the RCSB Protein Data Bank(PDB). We have chosen proteins with ID 4CS4 and 4D2I in our experiment. Figure 6.11(a) and (d) show the surface representations of proteins 4CS4 and 4D2I respectively. The green regions denote the particular regions we are interested in. (b) and (e) show the electrostatic surfaces of proteins 4CS4 and 4D2I respectively. The electrostatic properties of the protein are calculated by solving the Poisson–Boltzmann equation [2]. The zoom-in of the selected regions with electrostatic information are shown in (c) and (f). These subregions are extracted for the demonstration of our proposed parameterization methods.

To test our algorithm, we parameterize the selected subregion of each protein. The selected subregions of the two protein surfaces are shown in Figure 6.11 (a) and (b), which are marked in green. Denote the selcted green regions of the two protein surfaces by S_1 and S_2 respectively. S_1 and S_2 are shown more clearly in Figure 6.11 (c) and (f).

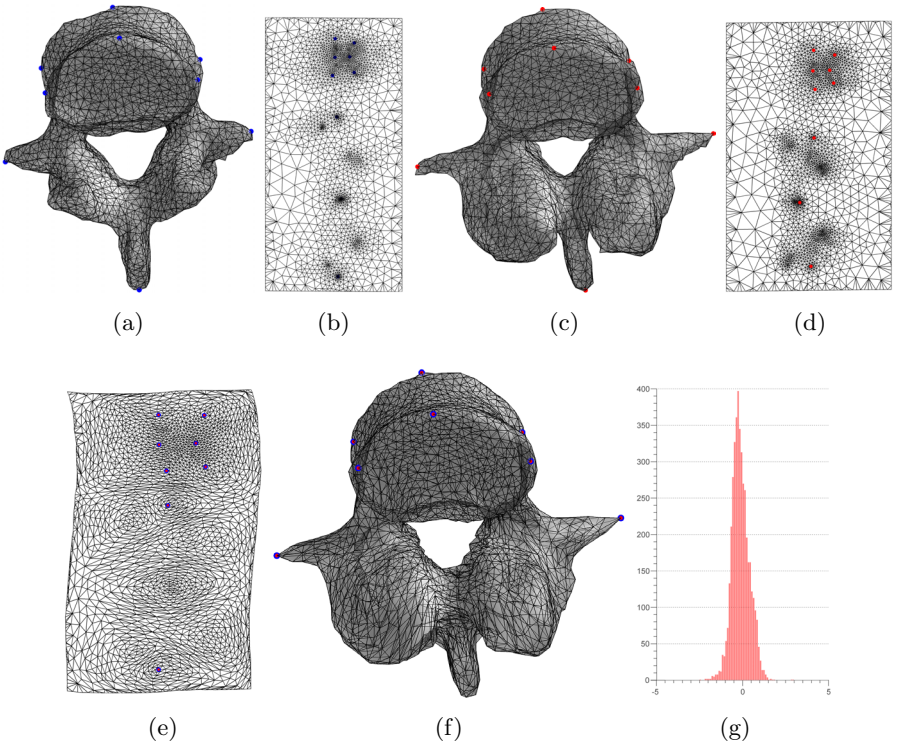

Fig. 6.10: *(a) shows the surface mesh of Vertebra bone A. Feature landmark points are marked as blue dots. (b) shows the conformal parameterization of bone A into its universal covering space. (c) shows the surface mesh of Vertebra bone B. Corresponding feature landmark points are marked as red dots. (d) shows the conformal paramterization of bone B into its universal covering space. (e) shows the landmark-aligned optimized parameterization, which minimizes both the conformal and area distortions. Using the composition map of the parameterizations, we deform bone A to bone B, which is shown in (f). (g) shows the histogram of the logarithmic Jacobian determinant of the overall mapping.*

Our goal is to look for an optimized parameterization of S_i $(i=1,2)$ such that the area of a selected subdomain Ω_i is preserved under the parameterization, while minimizing the conformality distortion. The subdomains Ω_i's of S_i's are shown in Figure 6.12 (a) and (c), which are regions colored in red on the surfaces. Corresponding landmarks are delineated on each surfaces, which are labeled as green dots. In this example, we aim to align landmarks onto consistent locations on the parameter domain, while preserving the area of the selected subdomains under the parameterization as good as possible. Denote the conformal parameterization of S_i by ϕ_i $(i=1,2)$. As before, we set $\lambda = \frac{\mathcal{A}(\Omega_i)}{\mathcal{A}(\phi_i(\Omega_i))}$ on Ω_i. The conformal parameterizations of Ω_1 and Ω_2 are shown in Figure 6.12 (b) and (d) respectively. The green dots denote the locations of landmarks on the conformal parameter domain. The purple and the blue colors indicate the positive and negative potential respectively. The distribution of the potential plays a significant role on the binding between proteins, defining mechanisms of protein-protein complex formation as well as the study of protein movements [29]. Note that the red regions Ω_i are squeezed on the conformal parameter domains in both cases. This hinders the visualization and shape comparison of protein structures on the 2D parameter domain.

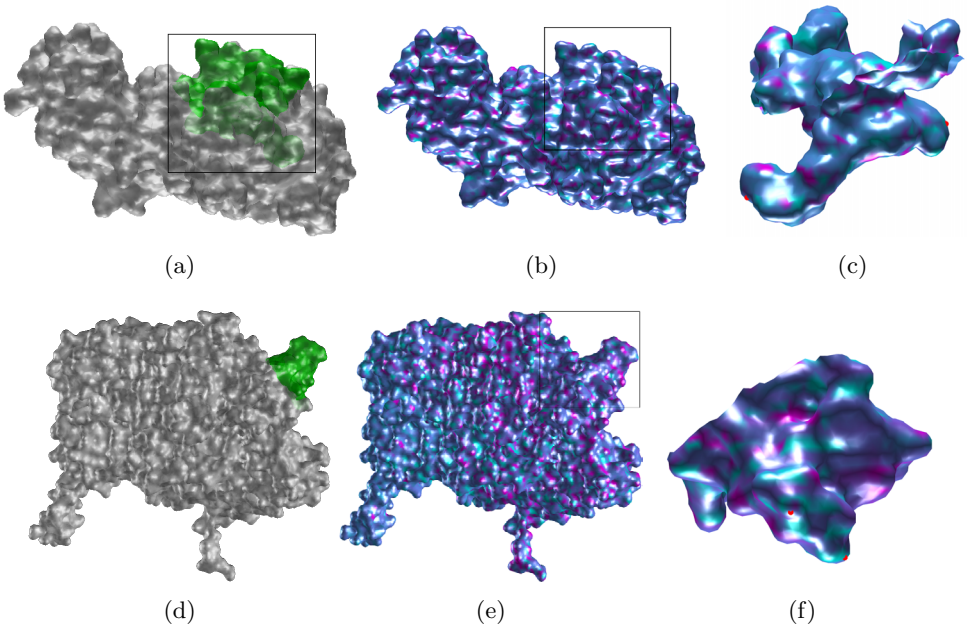

Fig. 6.11: *(a) and (d) show the surface representation of the proteins with ID 4CS4 and 4D2I respectively. The selected regions of interest are labeled in green. (b) and (e) show the electrostatic information of the proteins in (a) and (d). (c) and (f) show the zoom-in of the selected region of together with the corresponding electrostatic information in (b) and (e) respectively.*

Using our proposed algorithm, we aim to obtain protein surface parameterization, which minimizes area and conformality distortions.

In order to compare the two selected areas of the protein surfaces, we fix the parameter domain as a 2D rectangle of certain dimensions. Furthermore, we set $\alpha = 1$ and $\gamma = 0.1$ in this example. For S_1, we apply our proposed algorithm to compute an optimized conformal parameterization, which minimizes the area distortion of Ω_i as well as the conformality distortion under the parameterization. The parameterization result is shown in Figure 6.12(e) and (f). For S_2, we compute an optimized landmark-aligned conformal parameterization preserving the area of the selected subdomain Ω_2, such that corresponding landmarks are aligned to consistent locations as those in Figure 6.12(e) and (f). The parameterization result is shown in Figure 6.12(g) and (h). Note that corresponding landmarks are indeed aligned consistently. Also, unlike the conformal parameterizations, the selected (red) subdomains Ω_1 and Ω_2 are not squeezed on the parameter domain under the parameterizations. It demonstrates that our algorithm can produce optimized parameterizations, which gives a good balance between area and conformality distortions while aligning the prescribed landmarks consistently. This allows us to visualize the electrostatic information in the interested (red) regions on the 2D parameter domain more effectively. Figure 6.12(f) and (h) give a clearer visualization of the parameterized meshes, whose colormaps are given by their electrostatic information. The energies versus iterations of our algorithm to compute the parameterizations are shown in Figure 6.12(i) and (j) respectively.

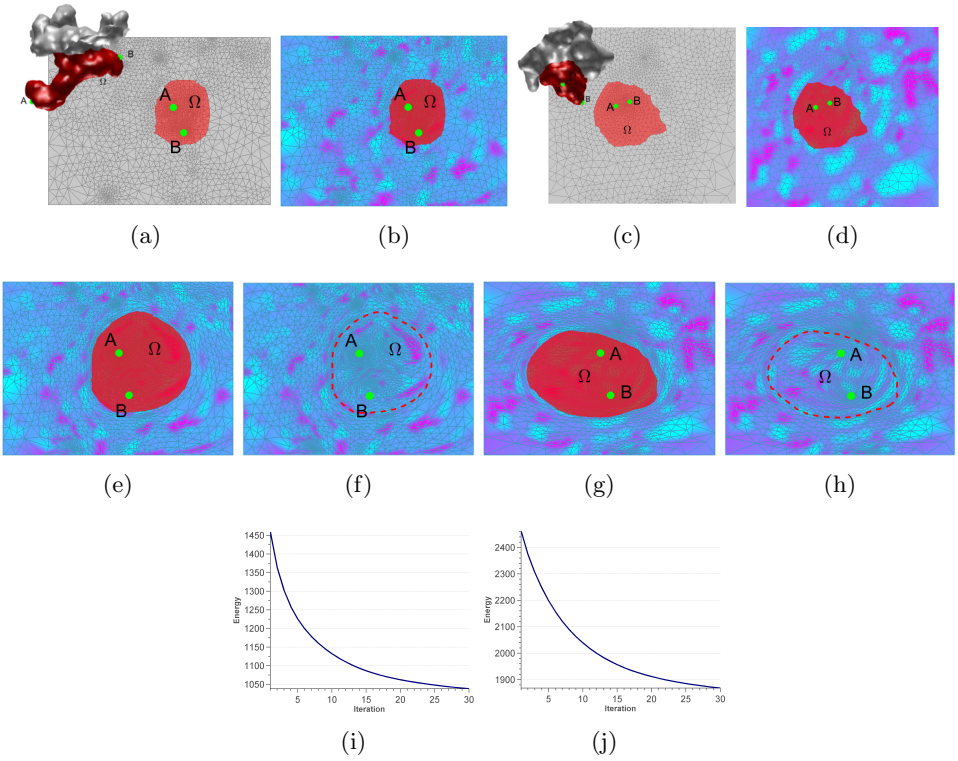

Fig. 6.12: *(a) and (c) show the surfaces of selected green regions (See Figure 6.11(a) and (d)) on the upper left corner and also their corresponding conformal parameterization. The sub-regions colored in red, are denoted as Ω_{S_1} and Ω_{S_2} respectively (We suppress the notation simply to Ω in the diagram for cleanliness). Two pairs of landmarks A and B are marked in green dots. (b) and (d) indicate the positive and negative potential by using purple and the blue colors respectively. (e) and (g) show the parameterization results. Note that due to the landmark criteria, the pairs of landmarks A and B are indeed aligned consistently. Also, unlike the conformal parameterizations, the red regions are not squeezed on the parameter domain under the parameterizations. (f) and (h) give a clearer visualization of the parameterized meshes. The energies versus iterations of our algorithm to compute the parameterizations are shown in (i) and (j) respectively.*

7. Conclusion

This paper presents a new approach to obtain a landmark-free or landmark-aligned surface parameterization which balances between the conformal and area distortions. Furthermore, the area distribution of the surface parameterization can be prescribed by users to fit into their applications. The main strategy is to minimize an energy functional consisting of the area mismatching term and the regularization term involving the Beltrami coefficient. The Beltrami coefficient measures the conformality distortion of the quasiconformal map. It also helps controlling the bijectivity and smoothness of the parameterization. Experiments have been carried out on both synthetic and real data. Results show that our proposed method can effectively control the area distribution as well as the conformality distortion of the parameterization. In the future, we plan to extend our proposed algorithm to 3D volumetric data and apply our proposed algorithm to medical imaging for diseases analysis.

Acknowledgment. Lok Ming Lui is supported by RGC GRF (Project ID: 401811).

REFERENCES

[1] F.L. Bookstein, *Principal warps - thin-plate splines and the decomposition of deformations*, IEEE Transactions on Pattern Analysis and Machine Intelligence, 11(6):567–585, 1989.

[2] T.J. Dolinsky, J.E. Nielsen, J.A. McCammon, and N.A. Baker, *PDB2PQR: An automated pipeline for the setup of poisson-boltzmann electrostatics calculations*, Nucleic Acids Research, 32(2):656–667, 2004.

[3] A. Dominitz and A. Tannenbaum, *Texture mapping via optimal mass transport*, IEEE Transactions on Visualization and Computer Graphics, 16(3):419–433, 2010.

[4] F.P. Gardiner and N. Lakic, *Quasiconformal Teichmüller Theory*, Amer. Math. Soc., 2000.

[5] J. Glaunès, A. Qiu, M.I. Miller, and L. Younes, *Large deformation diffeomorphic metric curve mapping*, International Journal of Computer Vision, 80(3):317–336, 2008.

[6] J. Glaunès, M. Vaillant, and M.I. Miller, *Landmark matching via large deformation diffeomorphisms on the sphere*, Journal of Mathematical Imaging and Vision, 20(1-2):179–200, 2004.

[7] X.F. Gu, Y. Wang, T.F. Chan, P.M. Thompson, and S.T. Yau, *Genus zero surface conformal mapping and its application to brain surface mapping*, IEEE Transaction on Medical Imaging, 23(8):949–958, 2004.

[8] X.F. Gu and S.T. Yau, *Computing conformal structures of surfaces*, Communication in Information System, 2(2):121–146, 2002.

[9] S. Haker, S. Angenent, A. Tannenbaum, R. Kikinis, and G. Sapiro, *Conformal surface parameterization for texture mapping*, IEEE Transactions on Visualization and Computer Graphics, 6(2):181–189, 2000.

[10] M.K. Hurdal and K. Stephenson, *Discrete conformal methods for cortical brain flattening*, Neuroimage, 45(1):S86–S98, 2009.

[11] A. Jacobson and O. Sorkine, *A cotangent Laplacian for images as surfaces*, ACM Transaction of Graphics, 25(3):646–653, 2012.

[12] M. Jin, J.H. Kim, F. Luo, and X.F. Gu, *Discrete surface ricci flow*, IEEE Transactions on Visualization and Computer Graphics, 14(5):1030–1043, 2008.

[13] K.C. Lam, X. Gu, and L.M. Lui, *Genus-one surface registration via teichmller extremal mapping*, Medical Image Computing and Computer-Assisted Intervention-MICCAI 2014. Springer International Publishing., 25–32, 2014.

[14] K.C. Lam and L.M. Lui, *Landmark and intensity based registration with large deformations via quasi-conformal maps*, SIAM J. Imaging Sci., 7(4):2364–2392, 2014.

[15] O. Lehto and K.I. Virtanen, *Quasiconformal mappings in the plane*, Die Grundlehren der mathematischen Wissenschaften in Einzeldarstellungen mit besonderer Berücksichtigung der Anwendungsgebiete, Springer, Berlin, Heidelberg, New York, Second Edition, 1973.

[16] B. Lévy, S. Petitjean, N. Ray, and J. Maillot, *Least squares conformal maps for automatic texture atlas generation*, ACM Transactions on Graphics (TOG), 21(3):362–371, 2002.

[17] Y. Lipman, *Bounded distortion mapping spaces for triangular meshes*, ACM Transactions on Graphics (TOG), 31(4):108, 1–13, 2012.

[18] L.M. Lui, X.F. Gu, and S.T. Yau, *Convergence analysis of an iterative algorithm for teichmller maps via harmonic energy optimization*, Mathematics of Computation, 2014.

[19] L.M. Lui, K.C. Lam, T.W. Wong, and X.F. Gu, *Texture map and video compression using Beltrami representation*, SIAM J. Imaging Sci., 6(4):1880–1902, 2013.

[20] L.M. Lui, K.C. Lam, S.T. Yau, and X. Gu, *Teichmuller mapping (t-map) and its applications to landmark matching registration*, SIAM J. Imaging Sci., 7(1):391–426, 2014.

[21] L.M. Lui, S. Thiruvenkadam, Y. Wang, T. Chan, and P. Thompson, *Optimized conformal parameterization of cortical surfaces using shape based matching of landmark curves*, Medical Image Computing and Computer-Assisted Intervention-MICCAI, Springer Berlin Heidelberg., 494–501, 2008.

[22] L.M. Lui, S.R. Thiruvenkadam, Y. Wang, P.M. Thompson, and T.F Chan, *Optimized conformal surface registration with shape-based landmark matching*, SIAM J. Imaging Sci., 3(1):52–78, 2010.

[23] L.M. Lui, Y.L. Wang, T.F. Chan, and P. Thompson, *Landmark constrained genus zero surface conformal mapping and its application to brain mapping research*, Appl. Num. Math., 57(5-7):847–858, 2007.

[24] L.M. Lui and C. Wen, *Geometric registration of high-genus surfaces*, SIAM J. Imaging Sci., 7(1):337–365, 2014.

[25] T.C. Ng, X.F. Gu, and L.M. Lui, *Teichmuller extremal map of multiply-connected domains using beltrami holomorphic flow*, J. Sci. Comput., 60:249–275, 2013.

[26] R. Schoen and S.T. Yau, *Lectures on Differential Geometry*, International Press, Cambridge, MA, 1994.

[27] C. Schüller, L. Kavan, D. Panozzo, and O. Sorkine Hornung, *Locally injective mappings*, Computer Graphics Forum, Blackwell Publishing Ltd., 32(5):125–135, 2013.

[28] F.B. Sheinerman, R. Norel, and B. Honig, *Electrostatic aspects of proteinCprotein interactions*, Current Opinion in Structural Biology, 10(2):153–159, 2000.

[29] N. Sinha and S.J. Smith-Gill, *Electrostatics in protein binding and function*, Current Protein and Peptide Science, 3(6):601–614, 2002.

[30] D. Tosun, M.E. Rettmann, and J.L. Prince, *Mapping techniques for aligning sulci across multiple brains*, Medical Image Analysis, 8(3):295–309, 2004.

[31] M. Vaillant and J. Glauns, *Surface matching via currents*, Information Processing in Medical Imaging, Springer Berlin Heidelberg, 381–392, 2005.

[32] Y.L. Yang, J. Kim, F. Luo, S.M. Hu, and X. Gu, *Optimal surface parameterization using inverse curvature map*, IEEE Transactions on Visualization and Computer Graphics, 14(5):1054–1066, 2010.

[33] W. Zeng and X. Gu, *Registration for 3d surfaces with large deformations using quasi-conformal curvature flow*, Computer Vision and Pattern Recognition (CVPR), 2011 IEEE Conference on., 2457–2464, 2011.

[34] W. Zeng, L.M. Lui, L. Shi, D. Wang, W.C. Chu, J.C. Cheng, and X Gu, *Shape analysis of vestibular systems in adolescent idiopathic scoliosis using geodesic spectra*, Medical Image Computing and Computer-Assisted Intervention-MICCAI. Springer Berlin Heidelberg, 538–546, 2010.

[35] X. Zhao, Z. Su, X.D. Gu, A. Kaufman, J. Sun, J. Gao, and F. Luo, *Area-preservation mapping using optimal mass transport*, IEEE Transactions on Visualization and Computer Graphics, 2838–2847, 2013.

[36] G. Zou, J. Hu, X. Gu, and J. Hua, *Area-preservation surface flatttening using lie advection*, Medical Image Computing and Computer-Assisted Intervention-MICCAI, Springer Berlin Heidelberg, 335–342, 2011.